

# Photoluminescence and X-ray photoelectron spectroscopic study of milled-ZnO material prepared by high energy ball milling technique

Wanichaya Mekprasart<sup>a</sup>, Balaji R. Ravuri<sup>b</sup>, Rattikorn Yimnirun<sup>c</sup>, Wisanu Pecharapa<sup>a,\*</sup>

<sup>a</sup> College of Nanotechnology, King Mongkut's Institute of Technology Ladkrabang, Bangkok, Thailand

<sup>b</sup> Gandhi Institute of Technology and Management, Hyderabad, Telangana 502329 India

<sup>c</sup> School of Energy Science and Engineering, Vidyasirimedhi Institute of Science and Technology, Rayong 21210 Thailand

\*Corresponding author, e-mail: wisanu.pe@kmitl.ac.th

Received 16 Oct 2019

Accepted 20 Mar 2020

**ABSTRACT:** Luminescence properties that are correlated to near band edge emission and defect-related emission of milled zinc oxide (ZnO) powder prepared by high energy ball milling technique are investigated. Commercial ZnO powder (particle size of 525 nm) was chosen as starting material in milling process to produce ultrafine ZnO powder. The milling process was carried out at different speeds; 0, 200, 400 and 600 rpm for 10 min. After milling at high speed, change in color of milled ZnO powder was clearly observed that could be due to the defects in ZnO structure induced by mechanical strain during milling process. Surface morphology of milled ZnO powder was monitored by field-emission scanning electron microscopy (FESEM). Element component and surface chemical states of the samples were analyzed by X-ray photoelectron spectroscopy (XPS). Optical property of milled samples was investigated by diffuse reflectance UV-Vis spectrometer. Meanwhile, room-temperature photoluminescence spectroscopy of the milled samples was performed. The milled ZnO particle size was distinctly decreased to ca. 200 nm affirmed by FESEM images. Photoluminescence (PL) spectra of milled ZnO sample showed two prominent emission bands; UV and visible region. Visible emission intensity increased with increasing milling speed that would be attributed to greater structural defects caused by high mechanical strain during milling process.

**KEYWORDS:** photoluminescence, X-ray photoelectron spectroscopy, milling, ZnO

## INTRODUCTION

Zinc oxide (ZnO) based material is greatly attractive as an effective semiconductor owing to its remarkable properties including direct wide band gap energy (3.37 eV), large exciton binding energy (60 meV), high electron mobility and good stabilities at high thermal and chemical environment [1, 2]. Regarding promising properties of ZnO nanostructures, various demanding utilizations are based on this material such as antibacterial material, photodetector, photocatalyst, light emitting diode, solar cell and optical waveguide [3–7]. Thus, the production of ultrafine ZnO powder in nanoscale has been focused and different synthesis methods have been proposed via both bottom-up and top-down processes. For bottom-up processes, final product of ZnO particles in different sizes and geometries can be obtained via chemical route using zinc precursor with reducing agents, depending on proper

precursor ratio, temperature and pressure. Different methods for the preparation of ZnO nanoparticles have been conducted including homogenous precipitation, spray pyrolysis, sol-gel network and hydrothermal method [8–11]. However, ZnO powder in commercial product is in the stable powder as oxide powder that is difficult to produce in nanosize structure. Therefore, top-down process such as mechanical milling process is an alternative route to reduce particle size and obtain amorphous or nanostructured material and meet the requirement of large-scale production. High energy ball milling process is one of effective technique in mechanical process for particle size reduction and deformed structure by impact force mechanism. The impact energy during this process provides greater effect on milled materials than conventional milling process resulting in further particle size reduction in shorter process time. During the milling process, particle fracture can be created by the collision among par-

ticles, balls and container wall leading to significant size reduction [12]. Meanwhile, the strain in the lattice and smaller pieces in the crystal occurring in this reaction can lead to the defects in its structure, for example, vacancies, dislocations, stacking faults and grain boundaries [13]. The effects of several parameters under milling process must be investigated such as operation time, milling speed, temperature, diameter and number of balls, container volume, and the mass ratio between balls and precursor weight [14]. Milling speed is considered to be a crucial parameter in milling process. It was reported that the particle size of alumina and magnesia mixture in high energy milling process was decreased gradually from 42.92 to 9.00  $\mu\text{m}$  under different milling speeds from 60–240 rpm within 3 h [15]. Meanwhile, color changing from white to yellow in ZnO powder can be occurred after milling at high speed. This result can be originated from thermal energy during milling operation leading to metallothermic reduction or compound formation and relevant structural defects. Therefore, further study in type of defects playing key role in color changing of ZnO powder is necessary.

In this work, size reduction of ZnO powder was carried out by mechanical high-energy ball milling method. The products of as-received and milled ZnO powder were characterized by mean of surface morphology, crystalline structure and particle size. Meanwhile, the defect and oxidation state of ZnO powder after milling process was deeply investigated by photoluminescence spectra and X-ray photoelectron spectroscopy technique to identify its origin in yellow appearance.

## MATERIALS AND METHODS

Commercial zinc oxide (ZnO) powder (Ajax Finechem Pty Ltd, Australia) with average particle size of 500 nm was used as starting material in high energy ball milling process. The as-received ZnO powder with powder to zirconia ball ( $\phi = 1$  mm, (Tosoh, Japan)) weight ratio of 1:30 was loaded in zirconia container. The milling speed was varied 200, 400 and 600 rpm for 10 min under ambient air atmosphere at room temperature. After that, ZnO powder was separated from the balls by sifting and baked at 100 °C for 2 h to remove moisturizer in the sample. The relevant properties of ZnO ultrafine powders after milling were investigated by various techniques. Crystalline structure and phase identification were characterized by X-ray diffractometer (XRD; Rigaku Smartlab) with  $\text{Cu K}\alpha$  ( $\lambda=0.154$  nm). Morphologies of before-/after-

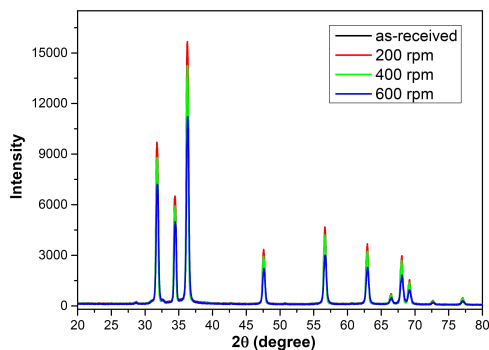


**Fig. 1** XRD patterns of as-received ZnO powder (black line, overlaid with red line), and milled-ZnO at 200 rpm (red line), 400 rpm (green line) and 600 rpm (blue line).

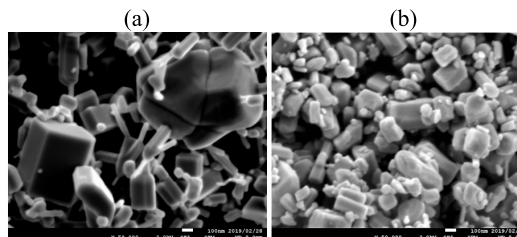


**Fig. 2** FESEM images ( $\times 50\,000$ ) of (a) as-received ZnO and (b) milled-ZnO at 600 rpm for 10 min.

milled products were monitored by field-emission scanning electron microscopy (FESEM; JEOL JSM-7001F). Chemical element and oxidation state on ZnO surface were observed by X-ray photoelectron spectroscopy (XPS) at beamline 5.2, Synchrotron Light Research Institute, Thailand. Meanwhile, crystalline defect of ZnO structure was analyzed by PL spectroscopy performed at room temperature using He-Cd laser with specific wavelength at 325 nm and diffuse reflectance spectroscopy technique.

## RESULTS

**Fig. 1** illustrates XRD patterns of as-received ZnO powder and ZnO powders milled at different speeds of 200, 400, and 600 rpm. The characteristic peaks situated at  $2\theta$  of 31.3°, 34.4°, 36.9°, 47.7°, 56.5° are associated to (100), (002), (101), (102) and (110) hexagonal wurtzite zinc oxide planes, respectively (JCPDS No. 36-1451). It is noticeable that the characteristic XRD peaks become broaden and their intensities drop significantly as the milling speed was beyond 400 rpm, implying reduction in their crystallite size. Their corresponding crystallite size was also calculated using well-known Scher-

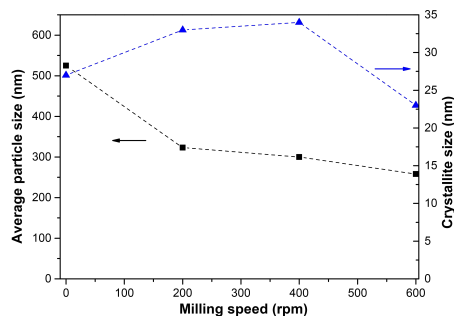


**Fig. 3** Average particle size (■) and calculated crystallite size (▲) of as-received ZnO (0 rpm) and milled-ZnO at speeds of 200, 400 and 600 rpm.

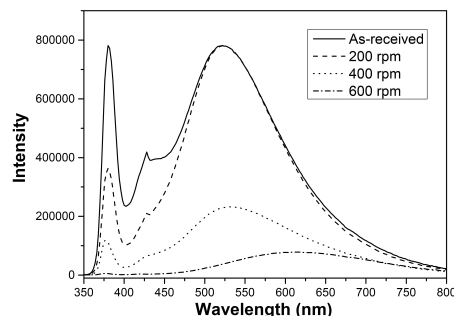


**Fig. 5** Photoluminescence of: as-received ZnO and milled-ZnO at speeds of 200, 400 and 600 rpm for 10 min.

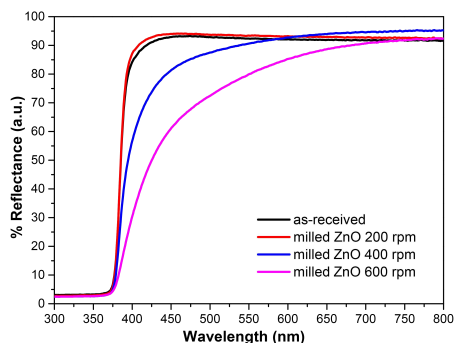


**Fig. 4** Diffuse reflectance spectra of as-received ZnO and milled-ZnO at speeds of 200, 400 and 600 rpm.

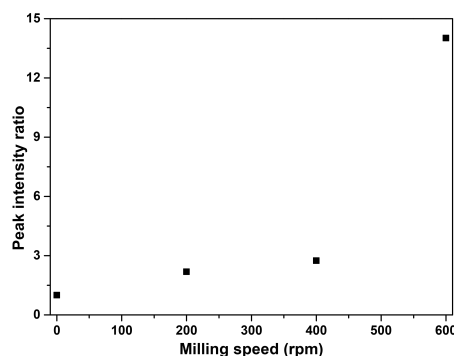


**Fig. 6**  $I_{VIS}/I_{NBE}$  peak intensity ratio of as-received ZnO and milled-ZnO at speeds of 200, 400 and 600 rpm for 10 min.

rer’s equation as illustrated in Fig. 3. The particle size values measured by particle size analyser and FESEM images are shown in Fig. 2. As observed in Fig. 2(a) and Fig. 2(b), significant reduction in its size was achieved after milling process. The average particle size of the powder was reduced considerably from ~530 nm for as-received sample to ~240 nm for ZnO sample milled at 600 rpm. In milling process, the increase in crystallite size at milling speed of 200 rpm and 400 rpm could be originated from the shear force between material and balls occurring at low milling speed that can lead to the agglomeration of ZnO particles and also the increase in crystallite size. Meanwhile, greater impact force during milling at higher milling speed beyond this certain speed could lead to crystal distortion and reduction in crystallite size.

Fig. 4 reveals the UV-Vis diffuse reflectance spectra of all samples. It is noticed that the reflectance in UV region ( $\lambda=300-375$  nm) of all samples is less than 5%, suggesting high UV absorptivity of the samples. The sharp reflectance edge can be

observed for all samples at  $\lambda \sim 375$  nm due to typical band gap of ZnO. Light with lower photon energy than its optical band gap is unable to be absorbed and photon-induced electron-hole pair is not generated, leading to high reflectivity of light in visible region. Moreover, it is obvious that the reflectance intensities of milled ZnO powders in visible region ( $\lambda=400-600$  nm) drops significantly with increasing milling speed, suggesting the enhancement in visible absorptivity of the milled samples. The color of the sample consequently changes from white for as-received ZnO to pale yellow appearance for the sample milled at 600 rpm (pictures are not shown). This feature could relate to the optical absorption of structural defect levels within ZnO band gap. Therefore, this result implies the creation of structural defects of the samples induced by mechanical milling process.

As seen in Fig. 5, PL spectra of as-received ZnO sample possesses prominent narrow peak positioned at about 375 nm that is corresponded to typical near-band-edge (NBE) emission of ZnO related to

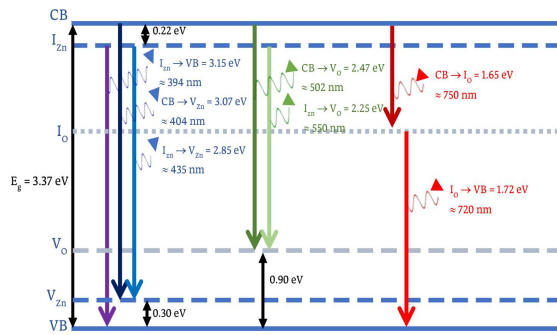


**Fig. 7** Energy levels of structural defects in ZnO and corresponding transition pathways responsible for its photoluminescence.

its typical band gap of 3.37 eV and is also in harmony with the reflectance spectra in Fig. 4 [16]. Moreover, there is an observable shoulder blue luminescence spectrum nearby NBE emission at around 420 nm in all samples which is related to the emission of zinc interstitial and zinc vacancy defect [17]. The broad emission covering the wavelength of 450–700 nm typically attributed to relevant defects including oxygen vacancy ( $\lambda_{\text{peak}} \sim 550$  nm) and oxygen interstitial ( $\lambda_{\text{peak}} \sim 600$  nm) whose peak is positioned at around 550 nm can be observed in all samples. This emission spectrum indicates the defects from oxygen vacancy which leads to the appearance of broad yellow emission relating to oxygen interstitial defect [18]. It is obvious that the intensities of both NBE and visible emission band decrease significantly as the milling speed increases. The peak intensity ratios of visible broad emission to near-band-edge emission ( $I_{\text{VIS}}/I_{\text{NBE}}$ ) of all samples indicating the qualitative and quantitative existence of defect-related emission compared to NBE emission are represented in Fig. 6. The  $I_{\text{VIS}}/I_{\text{NBE}}$  ratio is increased considerably as the milling speed increases. The intensity ratio of as-received ZnO is found to be about 1 and this ratio increases drastically to be 14 as the milling speed increases to 600 rpm. This phenomenon suggests that these structural defects could be increased by greater mechanical stress provided by milling process with higher speed. The PL spectra of all samples are accompanied with weak near infrared band peaked at 760 nm that is typically related to lattice disorder or defect along c-axis of ZnO [17].

## DISCUSSION

According to PL results, schematic picture of energy level positions that take responsibility of NBE and

visible emission is proposed as depicted in Fig. 7. There are various transition pathways of emission. Under laser excitation with photon energy greater than optical bandgap of ZnO ( $>3.37$  eV), electrons are excited to conduction band leaving holes in valence band. After few nanoseconds, electrons will recombine with holes and emit corresponding photon by different transition pathways. The NBE emission is from the recombination of electrons at the bottom of conduction band and holes at the uppermost of valence band ( $\text{CB} \rightarrow \text{VB}$ ). Many structural defect levels including zinc interstitial ( $I_{\text{Zn}}$ ), oxygen interstitial ( $I_{\text{O}}$ ), zinc vacancy ( $V_{\text{Zn}}$ ) and oxygen vacancy ( $V_{\text{O}}$ ) can be created during ball milling process.  $I_{\text{Zn}}$  and  $I_{\text{O}}$  are located at 0.22 eV and 1.65 eV below conduction band [19–21]. While  $V_{\text{Zn}}$  and  $V_{\text{O}}$  are typically situated at 0.30 eV and 0.90 eV over valence band [22, 23]. It is possible for excited electrons either from conduction band or captured electrons at ZnO to recombine with holes in valence band or captured holes at  $V_{\text{Zn}}$  to release blue emission with corresponding wavelengths of 394 nm ( $I_{\text{Zn}} \rightarrow \text{VB}$ ), 405 nm ( $\text{CB} \rightarrow V_{\text{Zn}}$ ) and 435 nm ( $I_{\text{Zn}} \rightarrow V_{\text{Zn}}$ ), ( $\lambda = 400\text{--}450$  nm). This emission band is clearly observed as a shoulder band nearby NBE. Furthermore, prominent broad green-yellow emission in PL spectra with increasing  $I_{\text{VIS}}/I_{\text{NBE}}$  for the milled samples is attributed to the emission from  $\text{CB} \rightarrow V_{\text{O}}$  ( $\lambda \sim 500$  nm) and  $I_{\text{Zn}} \rightarrow V_{\text{O}}$  ( $\lambda \sim 550$  nm). Meanwhile, the red-near infrared emission ( $\lambda = 600\text{--}750$  nm) could be originated from the  $\text{CB} \rightarrow I_{\text{O}}$  ( $\lambda \sim 750$  nm) and  $I_{\text{O}} \rightarrow \text{VB}$  ( $\lambda \sim 720$  nm) transition. In addition, there is significant red-shift of visible emission band to higher wavelength as the milling speed increases to 600 rpm. The behavior suggests that the greater mechanical impact can induce the shift in defect level of  $V_{\text{O}}$  and  $I_{\text{O}}$ , that is responsible for the shift of visible emission of milled ZnO.

XPS measurement of as-received ZnO and ZnO milled at 600 rpm was carried out to further investigate the chemical states in both samples. As shown in Fig. 8(a), the  $\text{Zn}2p_{3/2}$  peak positioned at 1021.4 eV with spin orbit splitting around 23 eV is a characteristic for divalence  $\text{Zn}^{2+}$  of Zn–O bond in ZnO lattice. Slight shift to higher binding energy than typical Zn in perfect lattice could contribute to Zn– $\text{O}_{\text{vacancy}}$  bonds in the inner surface without change in surface Zn state induced by milling process. It is implied that such defects should occur in the lattice rather than its surface [24]. In Fig. 8(b),  $\text{O}1s$  peak of oxygen in wurtzite ZnO lattice should typically be at around 529.8–529.9 eV [24–27].

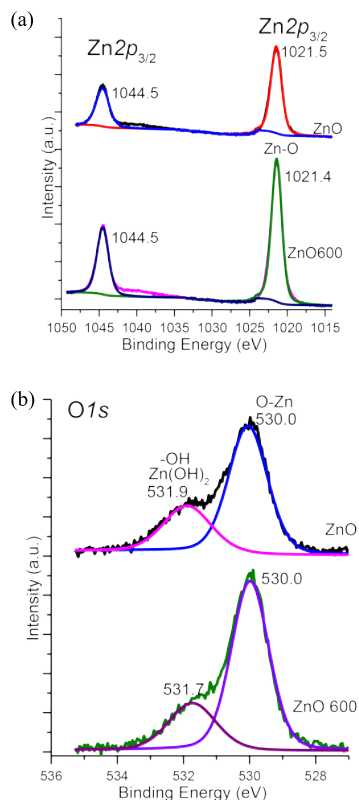


**Fig. 8** XPS spectra in (a)  $Zn2p_{3/2}$  and (b)  $O1s$  of as-received ZnO and milled-ZnO at 600 rpm.

Therefore, the peak at 530.0 eV with slight shift should be attributed to oxygen of Zn–O in ZnO lattice accompanying with small part of Zn–O<sub>vacancy</sub> at the inner surface, that is in accordance to the XPS spectra of  $Zn2p_{3/2}$  [28–30]. In addition, the  $O1s$  peak at 531.7 and 531.9 eV normally associates to oxygen of surface adsorbed hydroxy group -OH and zinc hydroxide  $Zn(OH)_2$  [24, 31–36]. However, there are no evidence of zinc hydroxide at  $Zn2p_{3/2}$  which should appear at around 1022.5–1023.4 eV [27, 37, 38]. This behavior suggests that the surface state is stable with insignificant influence by milling process.

## CONCLUSION

High energy ball milling method was employed to reduce particle size of ZnO powder. Its size can be reduced from 530 nm to 240 nm with the milling speed of 600 rpm for 10 min. However, color change from white to pale yellow occurred as the powder was milled at higher speed beyond 400 nm. Diffuse reflectance spectra of the milled sample in visible wavelength decreased significantly suggesting the

existence of structural defects created during milling process that are responsible for this color change. PL spectra of the samples can qualitatively describe the increase of structural defects including zinc interstitial, oxygen interstitial, zinc vacancy and oxygen vacancy by ball milling process. Meanwhile, XPS results suggest that such defects are mostly located in ZnO lattice rather than at the surfaces.

**Acknowledgements:** Ravuri would like to thank King Mongkut's Institute of Technology Ladkrabang (KMITL), Thailand for offering as Visiting Professor under Academic Melting Pot Program. Photoluminescence spectroscopy supported by the Frontier Research Center, Vidyasirimedhi Institute of Science and Technology and XPS experiment supported by Synchrotron Light Research Institute (Public Organization) beamline 5.3 XPS (BL5.3: SUT-NANOTEC-SLRI) are gratefully acknowledged.

## REFERENCES

1. Lanje AS, Sharma SJ, Ningthoujam RS, Ahn JS, Pode RB (2013) Low temperature dielectric studies of zinc oxide (ZnO) nanoparticles prepared by precipitation method. *Adv Powder Technol* **24**, 331–335.
2. Karimi M, Ezzati M, Akbari S, Lejbini MB (2013) ZnO microparticles, ZnO nanoparticles and  $Zn_{0.9}Cu_{0.1}O$  nanoparticles toward ethanol vapor sensing: A comparative study. *Curr Appl Phys* **13**, 1758–1764.
3. Xie YP, He YP, Irwin PL, Jin T, Shi XM (2011) Antibacterial activity and mechanism of action of zinc oxide nanoparticles against *Campylobacter jejuni*. *Appl Environ Microb* **77**, 2325–2331.
4. Boruah BD (2019) Zinc oxide ultraviolet photodetectors: rapid progress from conventional to self-powered photodetectors. *Nanoscale Adv* **1**, 2059–2085.
5. Tudose IV, Sucheana M (2016) ZnO for photocatalytic air purification applications. *IOP Conf Ser Mater Sci Eng* **133**, ID 12040.
6. Kwon DK, Porte Y, Myoung JM (2018) Fabrication of ZnO nanorods p-n homojunction light-emitting diodes using Ag film as self-doping source for p-type ZnO nanorods. *J Phys Chem C* **122**, 11993–12001.
7. Yu H, Wu Z, Dong Y, Huang C, Shi S, Zhang Y (2019) ZnO nanorod arrays modified with  $Bi_2S_3$  nanoparticles as cathode for efficient polymer solar cells. *Org Electron* **75**, ID 105369.
8. Oliveira APA, Hochepeid JF, Grillon F, Berger MH (2003) Controlled precipitation of zinc oxide particles at room temperature. *Chem Mater* **15**, 3202–3207.
9. Widiyandari H, Umiati NAK, Herdianti RD (2018) Synthesis and photocatalytic property of Zinc Oxide (ZnO) fine particle using flame spray pyrolysis method. *J Phys Conf Ser* **1025**, ID 12004.

10. Hasnidawani JN, Azlina HN, Norita H, Bonnia NN, Ratim S, Ali ES (2016) Synthesis of ZnO nanostructures using sol-gel method. *Procedia Chem* **19**, 211–216.
11. Wirunmongkol T, O-Charoen N, Pavasupree S (2013) Simple hydrothermal preparation of zinc oxide powders using Thai autoclave unit. *Enrgy Proced* **34**, 801–807.
12. Jayakumar OD, Salunke HG, Kadam RM, Mohapatra M, Yaswant G, Kulshreshtha SK (2006) Magnetism in Mn-doped ZnO nanoparticles prepared by a co-precipitation method. *Nanotechnology* **17**, 1278–1285.
13. Betancourt-Cantera JA, Sánchez-De Jesús F, Bolarín-Miró AM, Torres-Villaseñor G, Betancourt-Cantera LG (2019) Magnetic properties and crystal structure of elemental cobalt powder modified by high-energy ball milling. *J Mater Res Technol* **8**, 4995–5003.
14. Lemine OM, Louly MA, Al-Ahmari AM (2010) Planetary milling parameters optimization for the production of ZnO nanocrystalline. *Int J Phys Sci* **5**, 2721–2719.
15. Liu JH, Lv XJ, Li J, Zeng XP, Xu ZM, Zhang HL, Jiang LX (2016) Influence of parameters of high-energy ball milling on the synthesis and densification of magnesium aluminate spinel. *Sci Sinter* **48**, 353–362.
16. Lv JP, Fang MH (2018) Photoluminescence study of interstitial oxygen defects in ZnO nanostructures. *Mater Lett* **218**, 18–21.
17. Gomi M, Oohira N, Ozaki K, Koyano M (2003) Photoluminescent and structural properties of precipitated ZnO fine particles. *Jpn J Appl Phys* **42**, 481–485.
18. Verma K, Chaudhary B, Kumar V, Sharma V, Kumar M (2017) Investigation of structural, morphological and optical properties of Mg: ZnO thin films prepared by sol-gel spin coating method. *Vacuum* **146**, 524–529.
19. Willander M, Nur O, Sadaf JR, Qadir MI, Zaman S, Zainelabdin A, Bano N, Hussain I (2010) Luminescence from zinc oxide nanostructures and polymers and their hybrid devices. *Materials (Basel)* **3**, 2643–2667.
20. Zeng H, Cai W, Hu J, Duan G, Liu Ps, Li Y (2006) Violet photoluminescence from shell layer of Zn/ZnO core-shell nanoparticles induced by laser ablation. *Appl Phys Lett* **88**, ID 171910.
21. Lyons JL, Varley JB, Steiauf D, Janotti A, Van de Walle CG (2017) First-principles characterization of native-defect-related optical transitions in ZnO. *J Appl Phys* **122**, ID 035704.
22. Erhart P, Albe K, Klein A (2006) First-principles study of intrinsic point defects in ZnO: Role of band structure, volume relaxation, and finite-size effects. *Phys Rev B* **73**, ID 205203.
23. Rodnyi PA, Khodyuk IV (2011) Optical and luminescence properties of zinc oxide: a review. *Opt Spectrosc* **111**, 776–785.
24. Alshammari AS, Chi LN, Chen XP, Bagabas A, Kramer D, Alromaeh A, Jiang Z (2015) Visible-light photocatalysis on C-doped ZnO derived from polymer-assisted pyrolysis. *RSC Adv* **5**, 27690–27698.
25. Pradhan D, Leung KT (2008) Controlled growth of two-dimensional and one-dimensional ZnO nanostructures on indium tin oxide coated glass by direct electrodeposition. *Langmuir* **24**, 9707–9716.
26. Amor SB, Jacquet M, Fioux P, Nardin M (2009) XPS characterisation of plasma treated and zinc oxide coated PET. *Appl Surf Sci* **255**, 5052–5061.
27. Liangyuan C, Zhiyong L, Shouli B, Kewei Z, Dianqing L, Aifan C, Liu CC (2010) Synthesis of 1-dimensional ZnO and its sensing property for CO. *Sensor Actua B Chem* **143**, 620–628.
28. Chen M, Wang Z, Han D, Gu F, Guo G (2011) High-sensitivity NO<sub>2</sub> gas sensors based on flower-like and tube-like ZnO nanomaterials. *Sensor Actua B Chem* **157**, 565–574.
29. Malik G, Mourya S, Jaiswal J, Chandra R (2019) Effect of annealing parameters on optoelectronic properties of highly ordered ZnO thin films. *Mater Sci Semicond Proces* **100**, 200–213.
30. Pei Z, Ding L, Hu J, Weng S, Zheng Z, Huang M, Liu P (2013) Defect and its dominance in ZnO films: A new insight into the role of defect over photocatalytic activity. *Appl Catal B Environ* **142–143**, 736–743.
31. Lu W, Gao S, Wang J (2008) One-Pot Synthesis of Ag/ZnO self-assembled 3D hollow microspheres with enhanced photocatalytic performance. *J Phys Chem C* **112**, 16792–16800.
32. Du Y, Zhang MS, Hong J, Shen Y, Chen Q, Yin Z (2003) Structural and optical properties of nanophase zinc oxide. *Appl Phys A* **76**, 171–176.
33. Jing L, Xu Z, Shang J, Sun X, Cai W, Guo H (2002) The preparation and characterization of ZnO ultra-fine particles. *Mater Sci Eng A* **332**, 356–361.
34. Ramgir NS, Mulla IS, Pillai VK (2006) Micropencils and microhexagonal cones of ZnO. *J Phys Chem B* **110**, 3995–4001.
35. Al-Gaashani R, Radiman S, Daud AR, Tabet N, Al-Douri Y (2013) XPS and optical studies of different morphologies of ZnO nanostructures prepared by microwave methods. *Ceram Int* **39**, 2283–2292.
36. Zemlyanov DY, Savinova E, Scheybal A, Doblhofer K, Schlögl R (1998) XPS observation of OH groups incorporated in an Ag(111) electrode. *Surf Sci* **418**, 441–456.
37. Ahmed G, Hanif M, Mahmood K, Yao R, Ning H, jiao D, Wu M, Khan J et al (2018) Lattice defects of ZnO and hybrids with GO: Characterization, EPR and optoelectronic properties. *AIP Adv* **8**, ID 025218.
38. Wang M, Jiang L, Kim EJ, Hahn SH (2015) Electronic structure and optical properties of Zn(OH)<sub>2</sub>: LDA+U calculations and intense yellow luminescence. *RSC Adv* **5**, 87496–87503.